



Adjustment of river plume fronts during downwelling-favorable wind events

Runqing Lv^a, Peng Cheng^{a,*}, Jianping Gan^b

^a State Key Laboratory of Marine Environment Science, College of Ocean and Earth Sciences, Xiamen University, Xiamen, Fujian Province, 361102, China

^b Division of Environment, And Department of Mathematics, Hong Kong University of Science and Technology, Hong Kong, China

ARTICLE INFO

Keywords:

River plume
Down-welling favorable wind
Frontal adjustment
Symmetric instability

ABSTRACT

Downwelling-favorable winds modify the front structure of river plumes and are important for cross-shelf mass transport. To understand the adjustment process of river plume fronts in response to downwelling-favorable wind events, a series of generic numerical experiments were conducted. The adjustment of river plume fronts underwent three stages: destratification and restratification during the wind event and relaxation after the wind event. Ekman pumping drove a downwelling cross-shelf circulation that steepened the isohalines, leading to a destratification stage. As the wind continued blowing, instabilities occurred within the plume. The symmetric instability (SI) dominated and restratified the front during the remainder of the wind event, resulting in a restratification stage. After the wind event, baroclinic instabilities became dominant and further stratified the front. In the development of SI, the along-shelf freshwater transport was enhanced by the suppression of the bulge due to the down-front wind and provided a negative potential vorticity source that triggered and sustained the SI, together with the Ekman buoyancy flux. The result confirmed the importance of along-shelf processes in plume front adjustment. The timescale of the destratification process was related to the time taken by Ekman transport to reduce the width of the front. If the steepening time exceeds the duration of the wind event, the wind would be too weak to produce a well-mixed front, but instabilities would still develop and stratify the front during the restratification and relaxation stages.

1. Introduction

River plumes typically form a buoyant coastal current that flows tens to hundreds of kilometers in the direction of Kelvin wave propagation because of the earth's rotation. The coastal current acts as a conduit, transporting buoyancy and terrestrial materials from rivers to shelf seas, and has profound effects on circulation (Gan et al., 2009), biological productivity (Hickey et al., 2010) and coastal ecosystems (Jickells, 1998). Many studies have shown that winds are an important mechanism for altering the propagation and structure of river plumes. Chao (1988) identified two types of wind-induced responses of river plumes: the transport of salty water atop fresh water induced by onshore or downwelling-favorable winds, and the enhanced vertical current shear induced by offshore or upwelling-favorable winds. Onshore winds drive a cross-shelf flow with onshore flow in the upper layer and offshore flow in the lower layer that pushes the river plume to the coast (Choi and Wilkin, 2007; Fewings et al., 2008). Offshore winds reinforce offshore flow in the upper layer and drive the river plume away from the coast,

eventually bringing the plume to a steady state (Jurisa and Chant, 2013). Upwelling-favorable winds blow opposite the propagation direction of the plume, forcing the plume to become thinner and wider and to mix toward a critical depth. Through the Ekman straining mechanism, the cross-shelf buoyancy flux tends to enhance the stratification of the front and detach it from the coast (Fong et al., 1997; Fong and Geyer, 2001; Lentz, 2004).

The adjustments of buoyant plumes during downwelling-favorable winds, which have a down-front component, depend on the wind strength: moderate winds steepen the front, causing the plume to thicken, narrow and flow more rapidly along shelf, while strong winds produce a well-mixed water column and a wider plume front (Lentz and Largier, 2006). Using both analytical and numerical models, Williams et al. (2010) further illustrated that forced by persistent downwelling-favorable winds, the front undergoes a series of adjustments: Ekman transport mixes and steepens the isopycnals first in the surface then the bottom water column; eventually, the surface and bottom water columns merge, and the front reaches a quasi-steady state.

* Corresponding author.

E-mail address: pcheng@xmu.edu.cn (P. Cheng).

<https://doi.org/10.1016/j.csr.2020.104143>

Received 3 December 2019; Received in revised form 22 April 2020; Accepted 28 April 2020

Available online 8 May 2020

0278-4343/© 2020 Elsevier Ltd. All rights reserved.

When the water column on the landward side of the front becomes well-mixed, a weak recirculation flowing opposite the Ekman transport is developed because of the cross-shelf density gradient that generates a vertical geostrophic shear stress exceeding the wind stress (Moffat and Lentz, 2012; Chen and Chen, 2017). Forced by downwelling-favorable winds, the along-shelf transport of the river plume accelerates due to the enhanced cross-shelf pressure gradient and wind-driven flow (Whitney and Garvine, 2005). Also, the wind-forced cross-shelf circulation in the front region helps to generate a stable along-shelf jet (Johnson et al., 2001; Münchow and Garvine, 1993).

Instabilities have been found in coastal jets and upwelling fronts (Barth, 1994), but are seldom observed in river plumes (Horner-Devine et al., 2015). Hetland (2017) pointed out that unforced river plumes are typically too narrow to fit eddies of baroclinic instability, such that the plume may go unstable only under certain conditions that tend to broaden the plume and reduce vertical stratification. However, the existence of external forcing likely alters and generates complicated potential vorticity dynamics of fronts. Many open-ocean studies have revealed that fronts in the surface mixed layer are susceptible to submesoscale instabilities during down-front winds that advect denser over light water through Ekman flow and reduce the potential vorticity in the mixed layer (Taylor and Ferrari, 2010; Thomas and Taylor, 2010; Thomas, 2005). Submesoscale instabilities act to restratify the mixed layer and drive a forward cascade of energy from large to small scales, playing an important role in the dissipation of the ocean circulation energy (Boccaletti et al., 2007; Capet et al., 2008; D'Asaro et al., 2011). Through forced by downwelling-favorable winds that have a down-front component directed along the geostrophic shear, buoyant coastal currents also exhibit submesoscale instabilities (Allen and Newberger, 1996; Rogers-Cotrone et al., 2008). Using a series of idealized numerical experiments, Spall and Thomas (2016) further showed that the presence of the coast enhances submesoscale instabilities and results in more intense vertical motions and relative vorticities compared to a similar down-front wind in the absence of a coast.

Most previous studies on the adjustment of river plume fronts were two-dimensional analyses (e.g., in the cross-shelf direction), and neglected the direct effects of the along-shelf transport of buoyant water on the processes in the fronts. Because the along-shelf processes might play an important role in the front adjustment, it is the aim of this study to investigate the adjustment of a river plume front in response to downwelling-favorable winds in a three-dimensional framework. The main objectives are to understand the time-dependent, three-dimensional adjustment processes and to identify the forcing mechanisms for each adjustment stage. The results showed that the plume front undergoes a restratification adjustment stage after the front becomes well-mixed due to the symmetric instability (hereafter SI) triggered by the enhanced along-shelf freshwater transport.

The remainder of this paper is structured as follows. Section 2 describes the setup of the numerical model. Section 3 describes the adjustment processes of the plume front, estimates the time scale of destratification and identifies the role of instabilities in restratifying the front. Section 4 discusses the importance of along-shelf buoyancy transport in triggering instabilities and the energetics of the plume front during the downwelling-favorable wind event. Also, the influences of model configuration on the front adjustment were presented. Section 5 summarizes the main findings of this study.

2. Numerical model

A series of generic numerical experiments were carried out using the Regional Ocean Modeling System (ROMS), which is a free-surface, hydrostatic, primitive equations ocean model that uses stretched, terrain-following vertical coordinates and orthogonal curvilinear horizontal coordinates on an Arakawa C-grid (Shchepetkin and McWilliams, 2003). The model domain used in this study was designed as an estuary-shelf system (Fig. 1a). The portion of the domain corresponding to the

estuary was 50 km long to allow the estuarine circulation to be well developed. The flat-bottomed estuary channel was 6 km wide and 5 m deep. The shelf was 190 km wide and 400 km long. The water depth at the coast was 5 m, and the cross-shelf slope was constant. The model grid was 200 (cross-shelf, x direction) by 200 (along-shelf, y direction) by 40 (vertical, z direction) cells. The vertical layer was uniformly discretized. The horizontal grid spacing was 1 km in the cross-shelf direction and 2 km in the along-shelf direction. Because the full range of submesoscale variability extends down to 10–100 m, the 1 km horizontal grid resolution allows a “submesoscale-permitting” simulation, while a “submesoscale-resolving” simulation needs not only high horizontal grid resolution but also non-hydrostatic capability (McWilliams, 2019). Nonetheless, the ROMS model applied here can reveal the essential characteristics and the role of submesoscale instabilities in front dynamics as shown in latter analysis.

The eastern (sea-side) and western (shore-side) boundaries of the domain were closed. The radiation boundary condition was implemented for baroclinic velocities and tracers on the northern and southern boundaries following Matano and Palma (2013). The vertical mixing was computed using the two-equation turbulence closure $k - \omega$, and the background vertical eddy diffusivity was $5 \times 10^{-6} \text{ m}^2/\text{s}$. The Coriolis parameter f was $1 \times 10^{-4}/\text{s}$. The horizontal diffusivities were set to a constant value of $2 \text{ m}^2/\text{s}$. A weak ambient current with an amplitude of 0.05 m/s was set as a barotropic flow in the northern boundary to restrict the size of the bulge that appears near the river mouth. The salinity of the coastal ocean was 35 psu, and the temperature was 15°C . The buoyant inflow was specified at the head of the channel. The inflowing river water was prescribed to have zero salinity and a temperature of 15°C , identical to the background temperature set throughout the entire domain.

The model started from rest and ran without winds for 30 days to reach a relatively steady state, which is achieved when the cross-shelf location of the front is relatively stable (Fig. 1b). The model output at the steady state supplied the initial conditions for the simulations of downwelling-favorable wind events. Those wind events had a duration of 6 days with a constant wind speed specified from day 2 to day 7. The

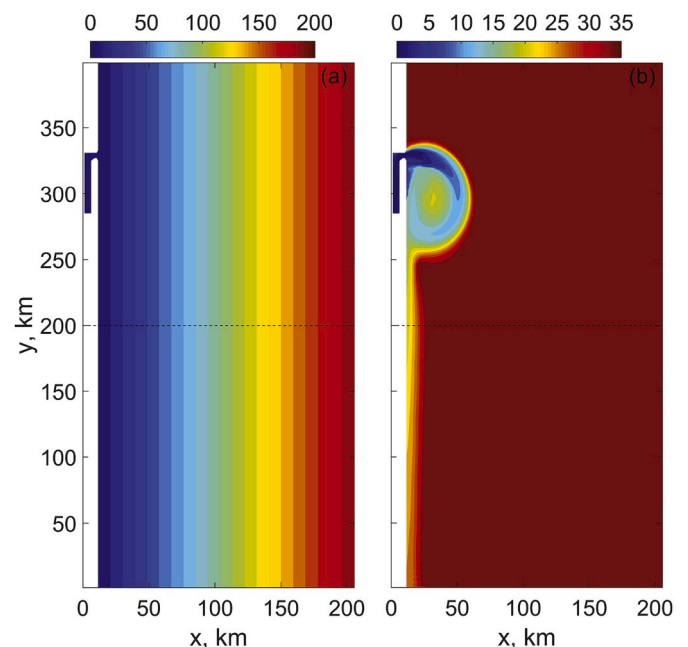


Fig. 1. Numerical model domain and depth (a), and the initial salinity field of the reference case (b). Freshwater enters the shelf at $y = 330$ km. The colors represent depth in units of meters in (a) and salinity in units of psu in (b). The dashed lines at $y = 200$ km indicate the location of the cross-shelf section selected for analysis.

wind speed increased linearly from zero to a constant value over 1 h at the end of day 1 and decreased linearly to zero over 1 h at the end of day 7. After the wind decayed, the plume was allowed to relax for 13 days. The entire simulation lasted 20 days. Six groups of numerical experiments were performed for a number of different values of wind speed, river discharge, and cross-shelf slope (Table 1). In each group, wind speed ranged from 1 to 20 m/s at an interval of 1 m/s. The wind stress was calculated using the bulk formula of Large and Pond (1981).

3. Results

As the river plume evolved to the steady state, a large bulge appeared near the river mouth and a narrow buoyant current propagated along the coast (Fig. 1b). Because the focus of this study is on the response of the river plume front to downwelling-favorable winds, a cross-shelf section at $y = 200$ km (Fig. 1) was selected, and the results of a reference case with a river discharge of $6000 \text{ m}^3/\text{s}$, a cross-shelf bottom slope of 0.001, and a spatially uniform wind speed of 6 m/s were chosen to illustrate the adjustment of the plume front.

3.1. Front adjustment

Before the onset of the wind event, the river plume was bottom-trapped (Fig. 2a). The along-shelf current of the plume was highly sheared (Fig. 2b) in accordance to that shown in Chapman and Lentz (1994). The salinity structure in the front formed a cross-shelf density gradient that drove a clockwise (facing upstream) circulation with seaward flow in the upper layer and landward flow near the bottom (Fig. 2a). The structure of river plume front was identified to undergo three stages in response to a downwelling-favorable wind event: destratification (day 1.0–2.3), restratification (day 2.3–7) and relaxation of the front after the wind event (day 7–20).

Ekman transport drove surface water landward, and thus the water surface elevation rose at the coast, resulting in a counterclockwise (facing upstream) downwelling cross-shelf circulation. As the wind continued to blow, the downwelling circulation overcame the clockwise circulation formed in the steady state and gradually dominated the cross-section (Fig. 2c). The cross-shelf circulation mostly steepened the isohalines and generated well-mixed surface and bottom Ekman layers. Wind-induced mixing also contributed to surface layer mixing, and its relative importance is addressed in the next section. The water column of the cross-section was separated into two layers by the halocline. The landward transport dominated the surface mixed layer, and the seaward transport dominated the lower layer. This cross-shelf circulation broke down the barrier effect of the front and facilitated the cross-shelf transport of riverine materials. The along-shelf current velocity accelerated in the surface mixed layer due to the wind stress, whereas the acceleration of the along-shelf current below the isohaline was less distinct, indicating that the influence of wind was limited to the surface layer (Fig. 2d).

Table 1
Configurations of the numerical experiments.

Group No.	Wind speed (m/s)	Wind duration (day)	River discharge (m^3/s)	Shelf slope	Other parameters
1	1–20	6	6000	0.001	
2	1–20	6	4500	0.001	
3	1–20	6	3000	0.001	
4	1–20	6	6000	0.002	
5	1–20	6	4500	0.002	
6	1–20	6	3000	0.002	
7	6	6	6000	0.001	80-km-long estuary channel
8	6	6	6000	0.001	Bathymetry disturbances
9	6	3,6,19	6000	0.001	

As the downwelling cross-shelf circulation continued to steepen the isohalines, the surface and bottom mixed layers merged on the landward side of the front to generate a well-mixed water column near the coast (Fig. 2e). The width of the plume was reduced. Because the stratification became weak in the plume region, the Ekman depth increased, which forced the downwelling circulation seaward to the offshore edge of the front. In the well-mixed region of the front, the cross-shelf circulation was clockwise, opposite to the Ekman transport. The generation of this clockwise circulation resulted from the competition between the geostrophic shear stress and wind stress. The former exceeded the latter because of the enhanced cross-shelf density gradient as a consequence of the steepening of isopycnals (Moffat and Lentz, 2012; Williams et al., 2010). The along-shelf current was further accelerated, the bottom counterflow disappeared and the along-shelf current touched the bottom. The downstream flow dominated the entire front region, and the maximum downstream transport appeared in the landward edge of the front where the water column was well-mixed (Fig. 2f).

With the continuous wind forcing, the front was restratified and grew sharply along with a reduction of plume width (Fig. 2g). The plume salinity was significantly reduced, and the lowest salinity near the coast dropped about 5 psu compared to the destratification stage. Apparently, the decrease in plume salinity resulted from the enhanced downstream transport of freshwater carried by the along-shelf current due to the continuous wind forcing. The freshwater transport within the plume was calculated and is given in section 4.1. Near the coast, the wind stress dominated the geostrophic stress and drove a downwelling circulation. In the front region (2–10 km offshore), two clockwise circulations were identified. The vertical motion associated with those circulations was characterized by subduction on the dense side of the front and upwelling along the frontal interface, indicating that strong fluid movement was aligned with the isopycnal. This cross-shelf circulation pattern agreed with the frontogenetic ageostrophic secondary circulation driven by wind-forced SI (Thomas and Lee, 2005). The along-shelf velocity of the plume continued to accelerate, and the core of the plume moved seaward (Fig. 2h).

The front relaxed after the decay of the wind event. The salinity in the cross-section increased due to the reduced downstream freshwater transport (Fig. 2i). The surface flow extended the plume seaward, and the landward bottom flow brought salty water into the front to increase stratification in the extended region. Near the coast, the cross-shelf circulation was clockwise. In the middle of the plume (2–6 km), the cross-shelf density gradient was weak and the circulation was counterclockwise. In the front region, the cross-shelf circulation flowed clockwise and stretched the isohalines, reinforcing stratification, and the along-shelf velocity of the plume slowed down (Fig. 2j).

The first adjustment stage, i.e. the destratification process, is consistent with the findings of previous studies and has been well-examined (Lentz and Largier, 2006; Williams et al., 2010; Moffat and Lentz, 2012), while the second adjustment stage, i.e. the restratification process, has not been well-identified and elaborated, and, therefore, is the focus of this study. In particular, the main efforts will be made to characterize those instabilities occurred after the first stage and to understand their roles in stratifying river plume fronts.

3.2. Destratification of the front

3.2.1. Drivers of destratification

Many processes can contribute to the destratification of the front. To examine the relative importance of each mechanism, we diagnosed the dominant terms of the potential energy anomaly (ϕ) equation (Burchard and Hofmeister, 2008; de Boer et al., 2008):

$$\frac{\partial \phi}{\partial t} = \frac{g}{D} \int_{-h}^{\eta} \bar{u} \frac{\partial \rho}{\partial x} dz + \frac{g}{D} \int_{-h}^{\eta} v \frac{\partial \rho}{\partial y} dz + \frac{g}{D} \int_{-h}^{\eta} K_v \frac{\partial \rho}{\partial z} dz + \dots \quad (1)$$

with ϕ defined as

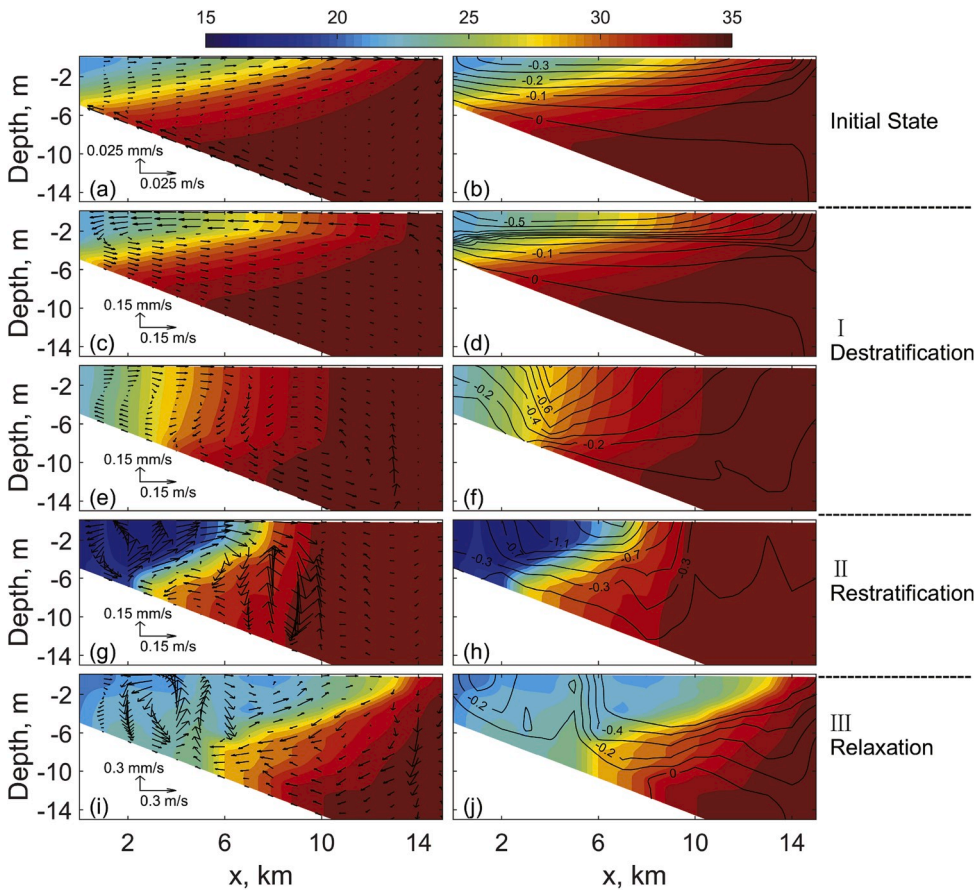


Fig. 2. Cross-shelf sections at $y = 200$ km showing salinity (see color contours in both columns), cross-shelf velocity (see arrows in the left column), and along-shelf velocity (see black contours in the right column) at times $t = 0.0$ (top row), 1.25 (second row), 1.75 (third row), 3.25 (fourth row), and 7.25 (bottom row) days after imposing a 6-day downwelling-favorable wind event with a wind speed of 6 m/s. From top to bottom, the first row represents the unforced stage, the second and third rows represent the destratification stage, the fourth row represents the restratification stage and the last row represents the relaxation stage. The cross-section is looking northward (upstream of the coastal current). Salinity is measured in psu and velocity in m/s. Only part of the cross-section is shown ($0 \text{ km} < x < 17 \text{ km}$). In the numerical experiment, river discharge is $6000 \text{ m}^3/\text{s}$ and the cross-shelf slope is 0.001.

$$\phi = \frac{1}{D} \int_{-h}^{\eta} gz(\rho - \rho) dz \quad (2)$$

where ρ is the water density, g is the gravitational acceleration, h is the mean water depth, η is the water surface elevation, $D = h + \eta$, K_v is the vertical eddy diffusivity, u and v are cross-shelf and along-shelf velocities, respectively, and $\langle \cdot \rangle$ represents depth average, for example, $\rho = \frac{1}{D} \int_{-h}^{\eta} \rho dz$, $\tilde{u} = u - \langle u \rangle$ (Simpson et al., 1990). The first term represents the cross-shelf straining, the second term represents the along-shelf advection and the third term represents the vertical mixing; other terms are omitted. The three terms in Eq. (1) averaged across the section from the coast to the seaward edge of the front (e.g. $0 \text{ km} < x < 17 \text{ km}$, where salinity is less than 34 psu) were compared to identify the relative contributions of these processes (Table 2). Note that ϕ_i is not completely balanced by the sum of the three terms due to the omission of other terms in Eq. (1). During the destratification stage, cross-shelf straining and vertical mixing reduced the stratification of the front (negative values), whereas along-shelf advection enhanced stratification and was negligible (one order smaller than the other two terms). The magnitude of cross-shelf straining was approximately fourfold that of vertical mixing, showing that the Ekman transport-induced cross-shelf

circulation was the major contributor to the destratification process.

3.2.2. Time scale of destratification

This steepening process during the destratification stage indicated a decrease in the potential energy in the cross-section of the river plume. Based on the above analysis, the major mechanisms that steepened the isohalines were cross-shelf straining and wind-induced mixing. Hence, the change in the potential energy anomaly of the cross-section is expressed as

$$\frac{d\phi}{dt} = \left(\frac{d\phi}{dt} \right)_{st} + \left(\frac{d\phi}{dt} \right)_w \quad (3)$$

where the subscript st represents the cross-shelf straining and w represents wind-induced mixing. $d\phi$ is approximately the potential energy anomaly at the unforced initial stage (ϕ_i) because the potential energy was nearly zero when the water column was well-mixed.

ϕ_i was estimated by simplifying the cross-section of the river plume to an idealized triangular shape with a linear increase in density across the plume (Fig. 3). Based on the geometric relationship, the density field of the profile can be expressed in a simple form:

$$\rho = \rho_c + \frac{\rho_o - \rho_c}{w} \left(x - \frac{w_r}{h_p} z \right). \quad (4)$$

Here, ρ_o is the density of oceanic water, ρ_c is the water density at the coast, w is the width of the front, w_r is the width from the foot of the front to the offshore edge of the front and h_p is the depth of the plume. Using Eq. (2), the potential energy anomaly at the initial stage is

$$\phi_i = g \frac{(\rho_o - \rho_s) w_r}{h_p} \frac{(\alpha w)^3}{48} \quad (5)$$

Table 2
Diagnostic of the potential energy equation during the destratification process.

	Maximum value (w/m^3)	Averaged value (w/m^3)
ϕ_i	-12×10^{-4}	-5.2×10^{-4}
Cross-shelf straining	-11×10^{-4}	-4.4×10^{-4}
Vertical mixing	-2.2×10^{-4}	-1.3×10^{-4}
Along-shelf advection	3×10^{-5}	2.6×10^{-5}

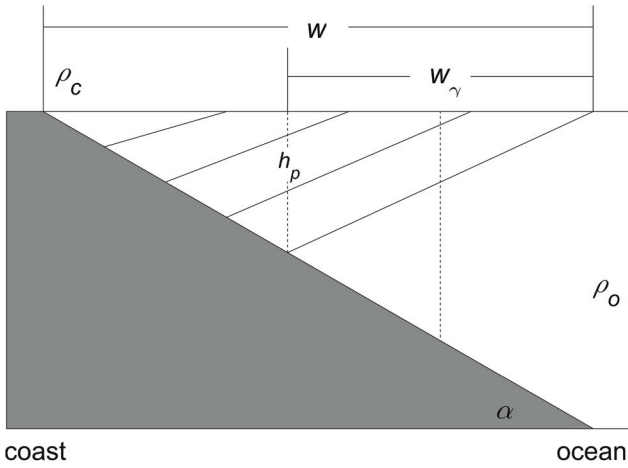


Fig. 3. Schematic of the simplified density profile in the unforced stage. The cross-shelf section is simplified to be a triangle and the coastal wall is ignored. ρ_c is the water density at the coast, ρ_o is the sea water density, α is the bottom slope, w is the width of the front, w_γ is the width from the foot of the front to the offshore edge of the front and h_p is the depth of the plume. The vertical dashed line that splits the triangle consisting of h_p and w_γ into halves is used to illustrate the factor 1/8 in the destratification time scale.

where α is the cross-shelf bottom slope. The power provided by the cross-shelf straining is

$$\left(\frac{d\phi}{dt}\right)_{st} = g \frac{\partial \rho}{\partial x} \int_0^w \int_{-h}^0 (u - u) z dz dx \quad (6)$$

where g is the gravitational acceleration and the cross-shelf velocity u is considered to be the Ekman transport velocity, i.e.,

$$u_E = \frac{\tau}{f \rho_o h_E} \quad (7)$$

Here, ρ_o ($= 1000 \text{ kg/m}^3$) is the reference water density, h_E ($= \sqrt{2A_v/f}$) is the Ekman depth, A_v is the vertical eddy viscosity, f is the Coriolis parameter and τ is the along-shelf wind stress. Combining Eqs. (6) and (7) gives the power of cross-shelf straining:

$$\left(\frac{d\phi}{dt}\right)_{st} = \frac{g \alpha^2 w^2 (\rho_o - \rho_c) \tau}{6f \rho_o h_E} \quad (8)$$

Following Simpson et al. (1990), the power generated by wind mixing is expressed as

$$\left(\frac{d\phi}{dt}\right)_w = \epsilon \tau w_s \quad (9)$$

where w_s is the along-shelf wind speed and ϵ is the mixing efficiency coefficient (taking a value of 0.02 here). Combining Eqs. ((3), (5), (8) and (9) gives the timescale of the steepening process:

$$T_D = - \frac{f \rho_o h_E g (\rho_o - \rho_c) w_\gamma (\alpha w)^3}{48 \epsilon h_p f \rho_o h_E \tau w_s + 8 h_p g \alpha^2 w^2 (\rho_o - \rho_c) \tau} \quad (10)$$

The relative importance of vertical mixing and cross-shelf straining in determining the destratification time scale can be compared through the ratio of the two terms in the denominator:

$$R = \frac{6 \epsilon \kappa \sqrt{\rho_a} \rho_o C_d w_s^2}{g \alpha^2 w^2 (\rho_o - \rho_c)} \quad (11)$$

Here, the wind stress is expressed in a quadratic form $|\tau| = \rho_a C_d w_s^2$, where $\rho_a = 1.22 \text{ kg/m}^3$ is the air density and C_d is a drag coefficient. Assuming a relatively strong wind with a speed of 20 m/s, $C_d = 0.00049 + 0.000065 w_s$ (Large and Pond, 1981). It gave an R of $O(10^{-3})$, showing that wind mixing can be neglected. Therefore, the timescale of

the steepening process can be simplified as

$$T_D = - \frac{f \rho_o h_E w_\gamma \alpha w}{8 h_p \tau} \quad (12)$$

To provide a prognostic estimate of the Ekman depth, a turbulent scaling, $h_E = \kappa u_* / f$, was used, where $u_* = \sqrt{|\tau|/\rho_o}$ and $\kappa = 0.4$ is the von Karman constant. The geometry parameters of the cross-front section were determined as follows: the salinity at the front edge (both surface and bottom) was chosen to be 34 psu; the distance from the coast to the surface edge of the front was the width of the front, w ; the depth of the bottom edge was the depth of the plume, h_p ; the distance from the bottom to surface edge of the front was w_γ ; and α was the shelf slope set in the model configuration. The destratification time scale was computed at the selected cross-section, which is located at $y = 200 \text{ km}$ for illustration. Using the numerical model output, the destratification time was also determined through the section-averaged potential energy anomaly that decreased to a minimum and then gradually increased during the wind event. The minimum value of the potential energy anomaly indicated the end of the destratification process, and thus the time from the onset of the wind to the time when the minimum potential energy anomaly occurred was considered to be the destratification time. In the reference case, ρ_o was 1025 kg/m^3 , w_γ was 9.5 km, w was 14 km and h_p was 9.5 m. The estimated time scale was 1.17 day, which agrees with the time scale obtained from the numerical model output (about 1.2 days).

Note that αw is approximate to the depth of the plume (e.g., h_p), and the time scale can be further simplified using Eq. (7):

$$T_D = \frac{w_\gamma}{8 u_E} \quad (13)$$

The physical meaning of the time scale is the time that the Ekman transport takes to suppress the front by a distance of w_γ (or to steepen the isohaline to become vertical). The factor of 1/8 indicated that the actual adjustment time was shorter. One reason is that the Ekman transport suppressed the front landward near the surface and simultaneously pushed the front seaward near the bottom such that the change in the plume width was less than w_γ . Another reason arose from the triangular approximation of the cross-section of the plume and the neglect of the vertical structure of the downwelling circulation. The two reasons led to a simple argument of the factor 1/8. The destratification time scale could be considered roughly as the time that it takes the Ekman transport to displace the isopycnals at the offshore edge of the plume to be vertical. The area associated with this displacement was approximately the upper (or lower) triangle formed by drawing a vertical isopycnal through the center of the sloping isopycnal (see the dashed vertical line in Fig. 3):

$$A = \frac{1}{2} \frac{w_\gamma}{2} \frac{h_p}{2} \quad (14)$$

and

$$T_D = \frac{A}{\tau / (\rho_o f)} = \frac{w_\gamma h_p}{8 u_E h_E} \quad (15)$$

The above argument simply demonstrated the source of the factor 1/8, but it appeared to be less strict than the estimation of the destratification time scale based on the removal of the potential energy anomaly by cross-shelf straining and wind mixing.

The numerical experiments of groups 1–6 were used to conduct an extensive examination of the destratification timescale. The prognostic time scales generally agreed well with the numerical results in addition to the outliers that represented the numerical experiments with a weak wind having a speed of 1.0 m/s (Fig. 4). The timescales of the outliers were larger than the wind duration (e.g., six days), indicating that those adjustments cannot be completed under weak wind forcing. This result was consistent with the prediction of the conceptual model proposed by

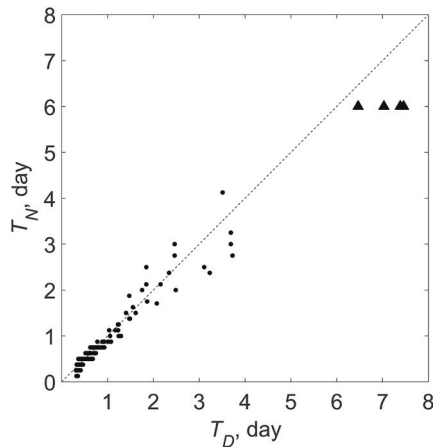


Fig. 4. Comparison of the destratification times between the scale analysis (T_D) and the numerical model output (T_N) for the steepening process. The outliers marked with triangles are data for the weak wind event having a wind speed of 1.0 m/s. The dashed line indicates $y = x$.

Lentz and Largier (2006) that weak winds cannot produce a well-mixed plume front.

3.2.3. Criterion for strong wind

A criterion that determines whether the wind is strong or weak is useful for predicting the existence of well-mixed plume front during a downwelling-favorable wind event. If the wind is strong, the steepening process can be completed during the wind event, i.e.,

$$T_D \leq T_w \quad (16)$$

where T_w is the duration of the wind event. Using the expression of T_D (e.g., Eq. (13)), the strong wind stress satisfied

$$\tau \geq \frac{f\rho_0 h_E w_\gamma \alpha w}{8h_p T_w} \quad (17)$$

For a wind event lasting six days, the critical wind stress was $1.8 \times 10^3 \text{ N/m}^2$. It was consistent with the weak wind numerical experiment in which the wind speed was 1.0 m/s ($\tau \approx 1.4 \times 10^3 \text{ N/m}^2$). Combining Eqs. (13) and (16) gives

$$u_E \geq \frac{w_\gamma}{8T_w} \quad (18)$$

This result showed that strong winds were those that drive a sufficiently large Ekman transport to suppress the plume front by a distance of w_γ for the entire duration of the wind. Therefore, both wind strength and duration determined whether the wind is strong.

3.3. Restratification of the front

3.3.1. Symmetric instability

A striking feature of the front adjustment during the restratification stage (and the relaxation stage) was the occurrence of instabilities that were illustrated using the surface salinity and mid-depth vertical velocity (Fig. 5). During the destratification stage, the river plume was stable, with a width of about 8 km and a smooth front edge (Fig. 5a). The vertical velocity had a magnitude of 10^{-2} mm/s and showed upwelling on the seaward side of the front and downwelling on the landward side (Fig. 5d), in accordance with the clockwise cross-shelf circulation. During the restratification stage, the bulge was suppressed, and the along-shelf freshwater transport was enhanced, resulting in a wider river plume with a width of about 20 km (Fig. 5b). The front became meandering, and wavelike disturbances appeared within the plume. The vertical velocity increased to 10^{-1} mm/s , one order larger than that during the destratification stage, and showed a complex subduction and

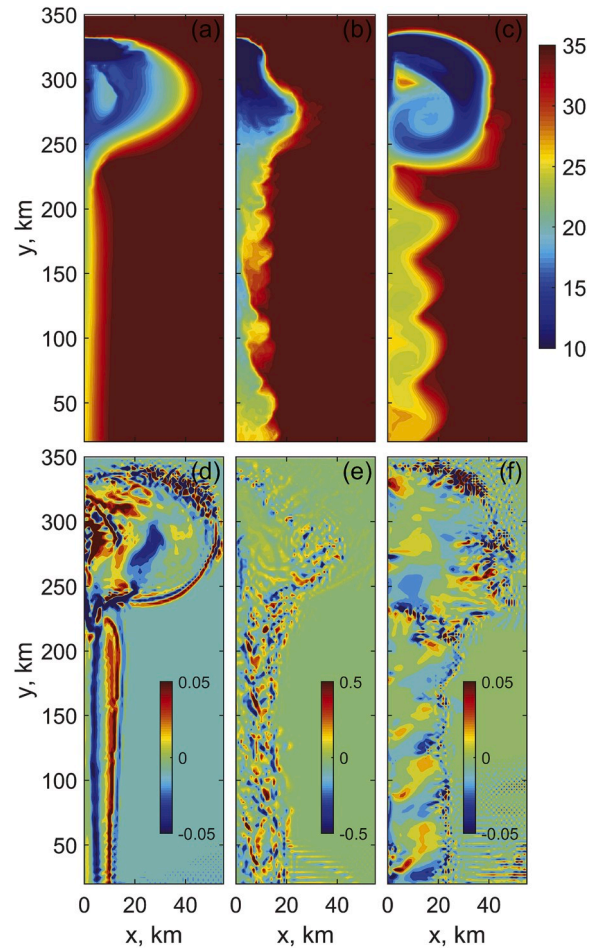


Fig. 5. Surface salinity (upper panel) and mid-depth vertical velocity (lower panel) at times $t = 1.25$ (right column), 6.25 (middle column) and 16.25 (left column) days to represent the destratification, restratification and relaxation stages, respectively. Salinity is measured in psu and velocity in mm/s. The results were taken from the reference experiment, which has a river discharge of $6000 \text{ m}^3/\text{s}$ and a cross-shelf slope of 0.001.

upwelling pattern (Fig. 5e). The cross-shelf circulations formed a number of discontinuous along-shelf rolls that were broken up by the wavelike disturbances. Referred to Fig. 2g, the cross-shelf structure of the vertical motion showed ageostrophic secondary circulations that tended to restore geostrophy and strengthen the front in consistent with the analysis of wind-forced front intensification developed by Thomas and Lee (2005), implying the occurrence of SI within the plume front.

A current is symmetrically unstable when its Ertel potential vorticity (PV),

$$q = (f\hat{k} + \nabla \times \mathbf{u}) \cdot \nabla b \quad (19)$$

takes the opposite sign of the Coriolis parameter, i.e. $q < 0$ in the northern hemisphere (Hoskins, 1974). Here, \mathbf{u} is the velocity vector, \hat{k} is a unit vector in the vertical and $b = g(\rho_0 - \rho)/\rho_0$ is the buoyancy. A parallel condition to $q < 0$ can be written in terms of the bulk Richardson number $Ri_B (= N^2 / (du_g/dz)^2)$, where \mathbf{u}_g is the geostrophic flow velocity vector) that is less than f/ζ_a , where $\zeta_a = f + \partial v/\partial x - \partial u/\partial y$ for the occurrence of SI (Haine and Marshall, 1998). The most unstable mode of SI developed when $0.25 < Ri_B < 0.95$ (Stone, 1966).

The PV averaged over the frontal region ($0 \text{ km} < x < 17 \text{ km}$ and $20 \text{ km} < y < 200 \text{ km}$) was initially positive and quickly decreased to become negative after the wind event started (Fig. 6b). During the restratification stage, the PV continued to decrease, reaching the

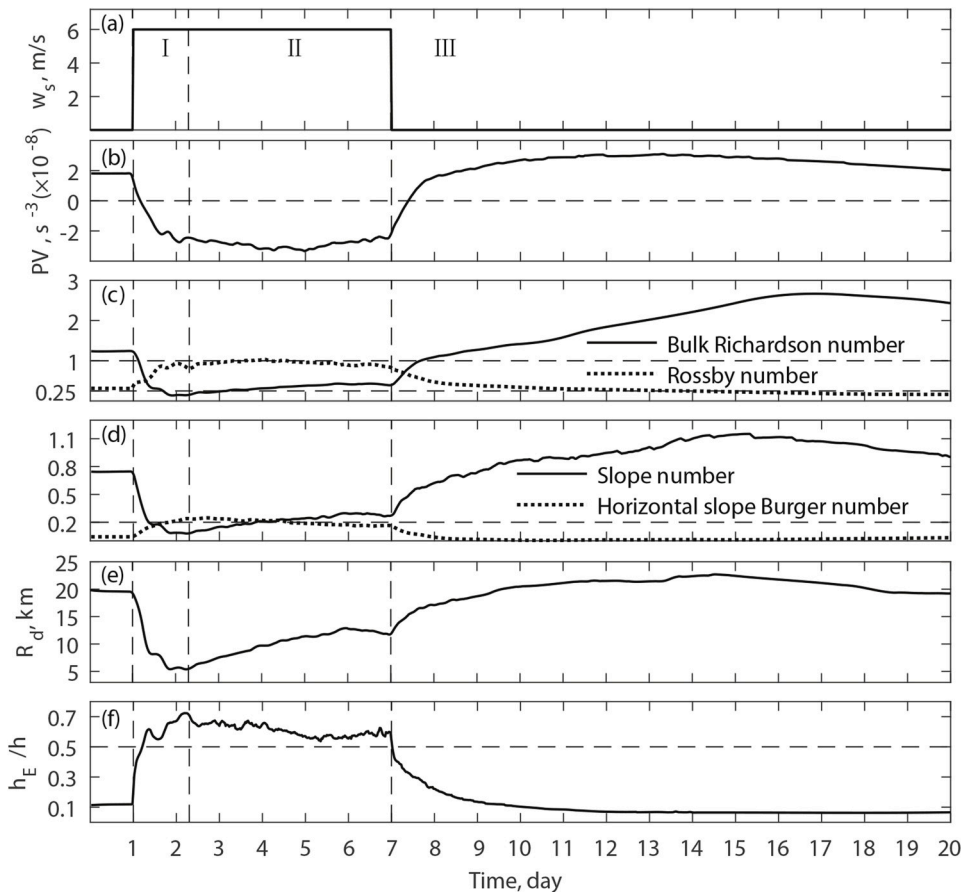


Fig. 6. The time series of (a) wind speed (w_s), (b) potential vorticity (PV), (c) bulk Richardson number and Rossby number, (d) Slope number and horizontal slope Burger number, (e) deformation radius (R_d) and (f) the ratio of the Ekman depth (h_E) to local water depth (h) in the reference numerical experiment. The parameters in (b)–(f) were averaged within $0 \text{ km} < x < 17 \text{ km}$ and $20 \text{ km} < y < 200 \text{ km}$. The vertical dashed lines indicate the destratification (I), restratification (II) and relaxation (III) stages. The horizontal dashed lines in (b) indicate a level of 0, and those in (c) indicate levels of 1 and 0.25.

minimum value around day 5, and then slightly increased. When the wind stopped, the PV became positive again. The bulk Richardson number dropped during the wind event and maintained values in a range of 0.25–0.4 during the restratification stage (Fig. 6c). Both the PV and bulk Richardson number favored the development of SI during the wind event. It is also noticed that SI was absent in the destratification stage and a discussion of the trigger of SI is given in section 4.1. SI is a type of submesoscale processes that are characterized by the Rossby number, $Ro \sim 1$ (McWilliams, 2016; Thomas et al., 2008). During the wind event, Ro increased, approaching 1 (Fig. 6c), supporting the occurrence of submesoscale instabilities. Hetland (2017) proposed that baroclinic instabilities grow in river plumes when the Rossby number $Ro \sim 1$ (McWilliams, 2016; Thomas et al., 2008). During the wind event, Ro increased, approaching 1 (Fig. 6c), supporting the occurrence of submesoscale instabilities. Hetland (2017) proposed that baroclinic instabilities grow in river plumes when the horizontal slope Burger number $S_H = Uf^{-1}W^{-1} \leq 0.2$, where U is a horizontal velocity scale. The S_H was around 0.2 during the wind event, indicating that the front was on the edge of baroclinic instability. The wave-like disturbances along the front edge of the surface salinity distribution supported the existence of baroclinic instabilities (Fig. 5c). Because the growth rate of SI is much larger than that of baroclinic instability (Taylor and Ferrari, 2010), SI developed rapidly and dominated the restratification stage, while baroclinic instability would further grow when the PV became positive after the wind event.

3.3.2. Eddy-induced restratification

Submesoscale instabilities act as a driver for restratifying the plume front (Spall and Thomas, 2016). Following a similar strategy of Taylor and Ferrari (2010), the buoyancy budget at the along-front averaged section was described by

$$\frac{\partial \bar{b}^y}{\partial t} = - \left(\bar{w}^y \frac{\partial \bar{b}^y}{\partial x} + \bar{w}^y \frac{\partial \bar{b}^y}{\partial z} \right) - \bar{v}^y \frac{\partial \bar{b}^y}{\partial y} - \bar{u}^y \cdot \nabla \bar{b}^y + \frac{\partial}{\partial z} \left(K_v \frac{\partial \bar{b}^y}{\partial z} \right) \quad (20)$$

where $-y$ denotes the average over the along-front (y) plane (e.g. in the

region of $20 \text{ km} < y < 200 \text{ km}$), and primes denote departures from the mean state. The advection terms were decomposed into mean and eddy components. On the right hand side of the equation, the first term (the two terms in the parenthesis) represents the mean cross-shelf advection, the second term represents the mean along-shelf advection, the third term represents the eddy advection and the last term represents the vertical diffusion.

A time average (from day 6.0–6.5) of Eq. (20) is shown in Fig. 7 to evaluate the relative importance of each term in the equation during the restratification stage. Both the mean cross-shelf circulation and the vertical diffusion reduced buoyancy near the surface and enhanced buoyancy in the lower layer, which tended to decrease stratification. The mean along-shelf advection freshened the plume near the coast and increased the cross-shelf buoyancy gradient. The eddy advection generally balanced the combined effect of the mean cross-shelf advection and vertical diffusion, and, therefore, is the driver of restratification.

The effect of instability eddies in producing the stratification of the plume front during the entire wind event was further examined using the spatially averaged buoyancy frequency equation that was obtained by vertically differentiating the buoyancy transport equation (e.g. Eq. (20)):

$$\frac{\partial}{\partial t} \overline{N^{2,y}} = - \frac{\partial}{\partial z} \left(\bar{w}^y \frac{\partial \bar{b}^y}{\partial x} + \bar{w}^y \frac{\partial \bar{b}^y}{\partial z} \right) - \frac{\partial}{\partial z} \left(\bar{v}^y \frac{\partial \bar{b}^y}{\partial y} \right) - \frac{\partial}{\partial z} \left(\bar{u}^y \cdot \nabla \bar{b}^y \right) + \frac{\partial}{\partial z} \frac{\partial}{\partial z} \left(K_v \frac{\partial \bar{b}^y}{\partial z} \right) \quad (21)$$

Here, $N^2 = \partial b / \partial z$, and the spatial mean ($-y$) takes both the x and y planes into account ($0 \text{ km} < x < 17 \text{ km}$ and $20 \text{ km} < y < 200 \text{ km}$). The four terms on the right side of the equation represent mean cross-shelf advection, mean along-shelf advection, eddy advection and vertical

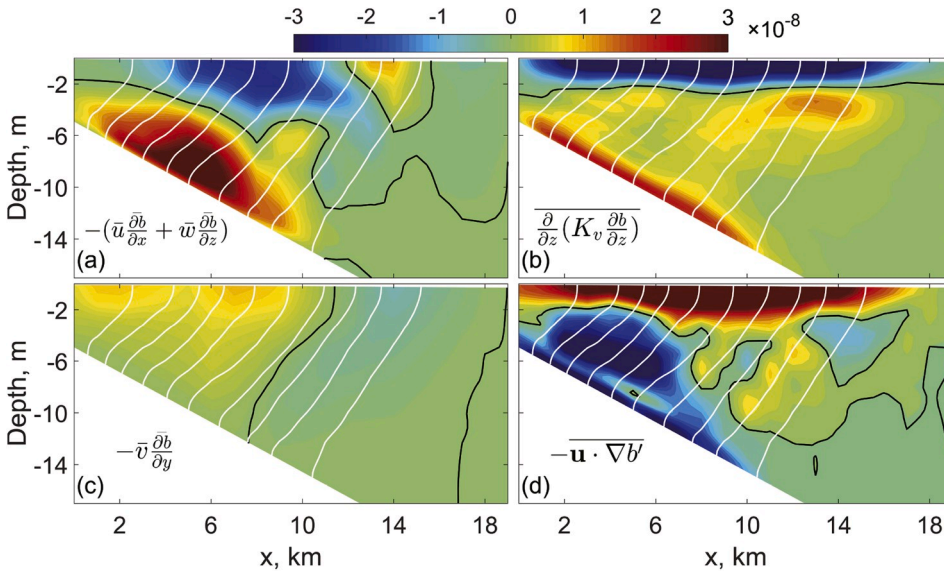


Fig. 7. Vertical profiles of the time-averaged buoyancy budget (from day 5.5–6.5) in the restratification stage: (a) mean cross-shelf advection, (b) mean along-shelf advection, (c) vertical diffusion and (d) eddy advection. The black lines indicate the zero contour, and the white lines represent the isohalines. The unit is m/s^3 . Only part of the section is shown ($0 \text{ km} < x < 19 \text{ km}$). The results were taken from the reference experiment, which has a river discharge of $6000 \text{ m}^3/\text{s}$ and a cross-shelf slope of 0.001.

diffusion. After the wind started, the eddy advection and mean along-shelf advection were always positive, enhancing stratification (Fig. 8), and the former dominated the restratification stage and the early relaxation. Vertical diffusion always reduced stratification. The mean cross-shelf advection reduced stratification during the wind event and dominated the destratification stage, then gradually increased stratification in later relaxation. The temporal evolution of the buoyancy frequency equation confirmed that the Ekman transport-induced cross-shelf circulation was the main driver of destratification and that the eddy advection was the main driver of restratification.

3.3.3. Relaxation of the front

During the relaxation of the front, the bulge was rebuilt and continued to grow. The along-shelf buoyant current became wider, with a width of about 25 km as a consequence of the extra freshwater input during the wind event. The disturbances along the front edge grew gradually and eventually formed four waves within 200 km in later relaxation (Fig. 5c). The vertical velocities became weaker, and the pattern was horizontally slanted toward the coast, with upwelling in the wave troughs and downwelling in the wave crests (Fig. 5f). The front waves exhibited a different type of instability. The PV became positive and Ri_B increased beyond 1.0 half a day after the wind stopped, indicating that symmetric instabilities tended to cease in the relaxation (Fig. 6b and c). S_H dropped toward extreme low values, a condition

favoring the development of baroclinic instability. Ro was much smaller than 1.0 in the relaxation, implying the development of mesoscale instabilities (Fig. 6c). As shown in the previous section, during the restratification stage, the front was marginally unstable of baroclinic instability that was overwhelmed by symmetric instability. In the relaxation of the front, baroclinic instability grew further and became dominant.

The unstable modes of baroclinic instabilities over a sloping bottom can be predicted using the diagram of linear theory (Blumsack and Gierasch, 1972; Hetland, 2017), which consists of two parameters: the slope parameter $\delta (= (N^2/M^2)\Lambda)$, where $M^2 = |\nabla_H b|$ is the magnitude of the lateral buoyancy gradients and Λ is the dimensional bottom slope, and the normalized wavenumber kR_d , where k is the wavenumber and $R_d (= NH/f)$, where H is the vertical length scale) is the local deformation radius. The slope parameter was positive in the reference experiment, representing a prograde slope with buoyant water in the shallower regions (Fig. 6d). The R_d was small during the wind event and increased to around 20 km, a length scale comparable to the plume width, in later relaxation (Fig. 6e). Specifically, δ was about 1.1 and R_d was about 22 km at day 16.25, which corresponds to Fig. 5c. According to the δR_d diagram (e.g. Fig. 3 in Hetland, 2017), for $\delta = 1.1$, the most unstable normalized wavenumber kR_d has a range from 2.7 to 3.3 that deduced the corresponding wave length was from 42 to 51 km. This result was consistent with the wave length of 50 km identified from the surface

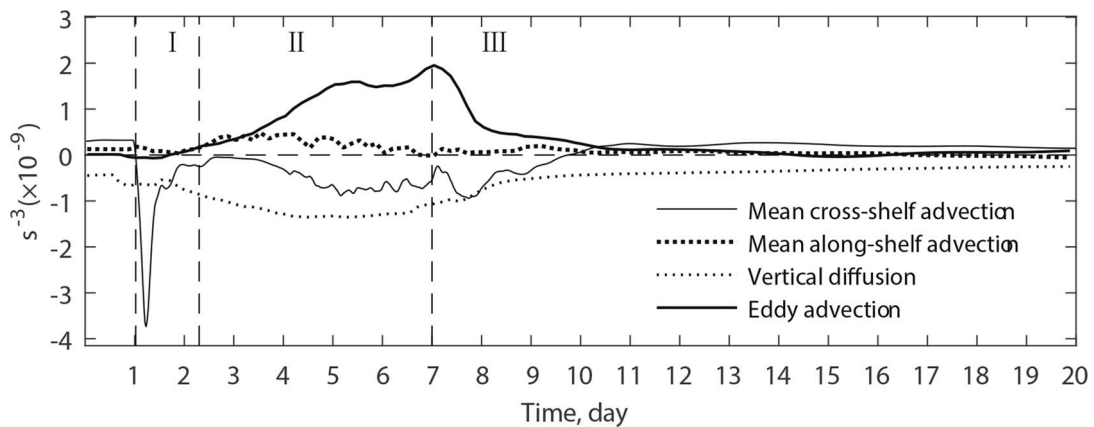


Fig. 8. The time series of the spatially averaged buoyancy frequency equation in the reference numerical experiment (averaged within $0 \text{ km} < x < 17 \text{ km}$ and $20 \text{ km} < y < 200 \text{ km}$). The vertical dashed lines indicate the destratification (I), restratification (II) and relaxation (III) stages.

salinity distribution (see Fig. 5c), and supported the dominance of baroclinic instability in the relaxation of the front. The relaxation was not completed because of the limited simulation duration. In reality, it will continue until the extra buoyancy obtained during the wind event was fully removed from the plume system.

4. Discussion

4.1. Drivers of symmetric instability

The surface buoyancy flux (note that it was not imposed in the numerical model) and Ekman buoyancy flux ($EBF = \frac{\tau}{\rho_0 f} \frac{\partial b}{\partial x} \Big|_{z=0}$) are the main processes that push the PV in the surface boundary layer toward the opposite of f (Thomas et al., 2013). However, the sign of the PV is a necessary but not sufficient criterion for forced SI because whether a force SI layer is active is determined by the competition between the convection and SI-induced frontal circulation (Taylor and Ferrari, 2010). The low PV layer in the surface boundary layer consists of two distinct layers: the convective layer is near the surface and remains relatively unstratified, while the forced SI is seen only below the convective layer. If the convective layer occupies the entire low PV layer, the forced SI is not expected to be active (Thomas et al., 2013). Unlike the open ocean, which has a surface boundary layer of hundreds of meters, river plume fronts are typically restricted by shallow water depth. Forced by downwelling favorable winds, the Ekman transport drove a cross-shelf circulation forming a convective layer that could occupy the entire water column (see Fig. 2c) and suppress SI during the destratification stage even through the PV was negative (Fig. 6b). The landward limit of the Ekman transport-induced cross-shelf circulation is at the location where the water depth is about twice the Ekman depth. During the destratification stage, as the stratification was decreasing, the Ekman depth increased such that the two-layer Ekman transport-induced cross-shelf circulation gradually moved seaward. This can be seen from the ratio between the Ekman depth (h_E) and the local water depth (h) that exceeded 0.5 and reached a maximum value of 0.7 at the end of the destratification stage (Fig. 6f). When the front tended to be well-mixed, the cross-shelf circulation as well as the convective layer

were pushed to the seaward side of the front (Fig. 2e), and the SI was able to dominate the frontal region. However, the seaward migration of cross-shelf circulation reduced the buoyancy transfer in the landward region of the plume front because EBF acts on the plume through the Ekman-induced cross-shelf circulation. Therefore, the SI could not be sustained unless an additional buoyancy flux was available to further extract the PV from the plume front.

The restratification stage started after the front became well-mixed and coincided with an abrupt increase in the along-shelf freshwater flux, Q_f , which was calculated following Fong and Geyer (2002):

$$Q_f = \iint v \frac{S_o - S}{S_o} dx dz \quad (22)$$

where s is salinity, s_o ($= 35$ psu) is the ambient oceanic water salinity and the integration is taken across the section from the coastline to $x = 17$ km and averaged from $y = 20$ km to $y = 200$ km (Fig. 9a). Before the onset of the wind event, the Q_f was about 32% of the river discharge ($6000 \text{ m}^3/\text{s}$), as most freshwater was stored in the bulge. The downwelling favorable wind accelerated the coastal current and suppressed the bulge, leading to enhanced along-shelf freshwater transport that exceeded the river discharge and reached a maximum value of $13,000 \text{ m}^3/\text{s}$ in the restratification stage. After the wind event, the bulge was rebuilt, and Q_f decreased to its initial value.

The influence of the along-shelf buoyancy source on the PV of a water body in river plumes can be illustrated by decomposing the PV into two terms (refer back to Eq. (19)):

$$q = q_{vert} + q_{bc} \quad (23a)$$

$$q_{vert} = \zeta_a N^2 \quad (23b)$$

$$q_{bc} = \left(\frac{\partial u}{\partial z} - \frac{\partial w}{\partial x} \right) \frac{\partial b}{\partial y} + \left(\frac{\partial w}{\partial y} - \frac{\partial v}{\partial z} \right) \frac{\partial b}{\partial x} \quad (23c)$$

Here, q_{vert} is associated with the vertical component of absolute vorticity and stratification, and q_{bc} is associated with the horizontal components of the vorticity and buoyancy gradients (Thomas et al., 2013). The along-shelf freshwater flux, on the one hand, increased stratification, leading to a larger positive q_{vert} ; on the other hand,

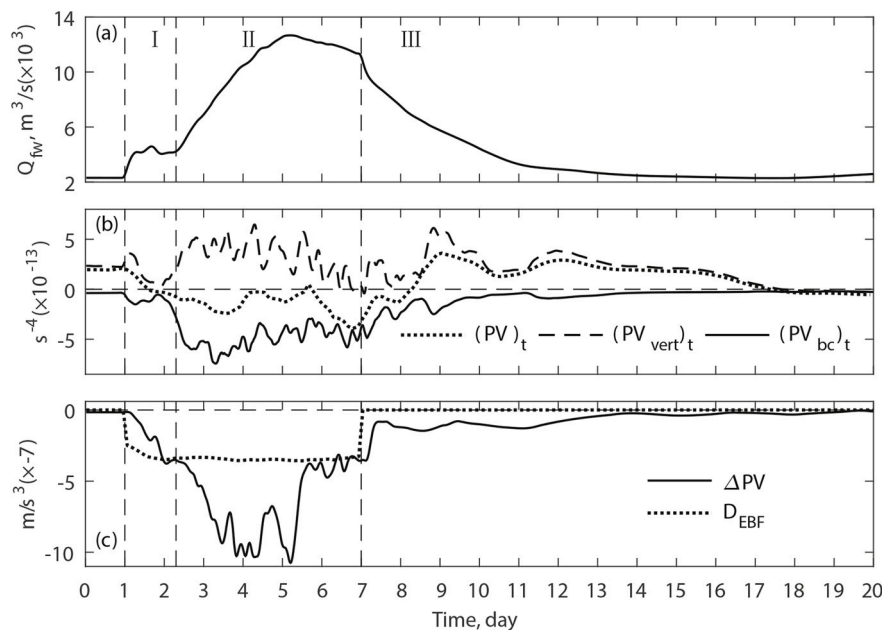


Fig. 9. The time series of the (a) downshelf freshwater flux; (b) potential vorticity (q) and its vertical (q_{vert}) and horizontal (q_{bc}) components; and (c) the Ekman buoyancy flux (D_{EBF}) and net along-shelf potential vorticity flux (ΔPV). The parameters were averaged within $0 \text{ km} < x < 17 \text{ km}$ and $20 \text{ km} < y < 200 \text{ km}$. The dashed vertical lines indicate the destratification (I), restratification (II) and relaxation (III) stages.

increased the horizontal buoyancy gradients, leading to a larger negative q_{bc} . The combined effect of the two components determines the contribution of the along-shelf freshwater flux to the PV. Using the buoyancy transport equation, the time rate of change in the PV due to the along-shelf advection of buoyancy (e.g. $v\partial b/\partial y$) reads

$$\frac{\partial q_{vert}}{\partial t} = -\zeta_a \frac{\partial}{\partial z} \left(v \frac{\partial b}{\partial y} \right) \quad (24a)$$

$$\frac{\partial q_{bc}}{\partial t} = - \left(\frac{\partial u}{\partial z} - \frac{\partial w}{\partial x} \right) \frac{\partial}{\partial y} \left(v \frac{\partial b}{\partial y} \right) - \left(\frac{\partial w}{\partial y} - \frac{\partial v}{\partial z} \right) \frac{\partial}{\partial x} \left(v \frac{\partial b}{\partial y} \right) \quad (24b)$$

A diagnostic of the two PV components showed that q_{vert} was positive and q_{bc} was negative during the simulation (Fig. 9b). The sum of the two terms was negative during the restratification stage, indicating that the along-shelf advection of freshwater acts as a driver in the destruction of the PV of the water body.

The relative importance of the PV sources was examined based on the PV conservation equation

$$\frac{\partial q}{\partial t} = -\nabla \cdot \mathbf{J} \quad (25)$$

where the PV flux is

$$\mathbf{J} = u\mathbf{q} - \nabla b \times \mathbf{F} - (\widehat{f}\mathbf{k} + \nabla \times \mathbf{u})\mathcal{D} \quad (26)$$

Here, \mathbf{F} represents the frictional forces and $\mathcal{D} (= Db/Dt)$ represents the diabatic processes (Haynes and McIntyre, 1987; Marshall and Nurser, 1992). Integrating Eq. (26) over a portion of the coastal front region of which the volume is V gives

$$\frac{\partial}{\partial t} \iiint_V q dV = - \oint_A [uq - \nabla b \times \mathbf{F} - (\widehat{f}\mathbf{k} + \nabla \times \mathbf{u})D] dA \quad (27)$$

The bounding surface A of the front region is made up of six parts (Fig. 10): two isopycnal surfaces (i.e. A_{land} and A_{sea} at s_1 and s_2 isohaline surfaces), two cross-front sections (i.e. upstream cross-section A_{up} and downstream cross-section A_{down}), one surface and one bottom. For such a volume, no PV is fluxed through the isopycnal surfaces (i.e. A_{sea} and A_{land}) according to the ‘‘impermeability theorem’’ of Haynes and McIntyre (1987), and through the seabed. Because diabatic processes were not included in the model, \mathcal{D} is zero. The Ekman buoyancy flux and the along-shelf advection of PV flux (i.e. uq) through the cross-sections (i.e. A_{up} and A_{down}) are the two drivers that destruct the PV of the volume.

The EBF is expressed as a diabatic process following Thomas (2005)

$$\mathcal{D}_{EBF} = -\frac{EBF}{h} \quad (28)$$

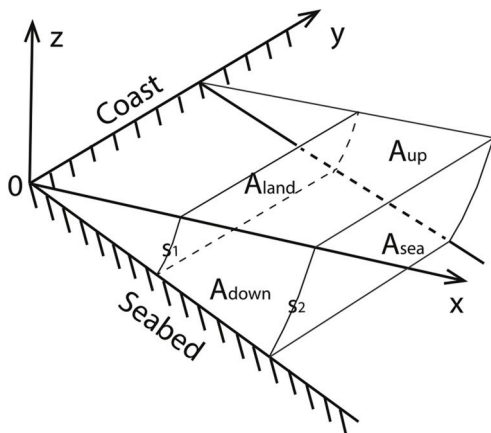


Fig. 10. Schematic of a control volume of a coastal buoyant current. A_{land} and A_{sea} are isopycnal surfaces with salinity of s_1 and s_2 . A_{up} and A_{down} are the upstream and downstream cross-sections of the volume.

and the net along-shelf PV flux is the difference of PV flux through A_{up} and A_{down}

$$\Delta PV = FPV_{down} - FPV_{up} \quad (29)$$

Here, FPV is the PV flux through a cross-section, and the subscripts *down* and *up* represent the downstream and upstream cross-sections. The spatially averaged \mathcal{D}_{EBF} slightly increased during the wind event as the cross-shelf buoyancy gradient increased (Fig. 9c). The enhanced along-shelf buoyancy flux provided low PV water, leading to negative net along-shelf PV flux. The evolution of ΔPV was similar to that of Q_f : it increased and exceeded \mathcal{D}_{EBF} during the restratification stage, showing that both EBF and the along-shelf PV flux acted as drivers of SI.

4.2. Energetics of the front

The role of instabilities in energy production and transfer can be tested by comparing the dominant terms in the perturbation kinetic energy budget. Following Barth (1994) and Thomas et al. (2013), the evolution of eddy kinetic energy ($EKE = (u'^2 + v'^2)/2$) is governed by the following equation:

$$\begin{aligned} \frac{D}{Dt} EKE = & \underbrace{-\overline{v'w'} \frac{\partial \overline{v'_g'^{xy}}}{\partial z}}_{GSP} - \underbrace{\left[\overline{v'w'} \frac{\partial (\overline{v'^{xy}} - \overline{v'_g'^{xy}})}{\partial z} + \overline{u'w'} \frac{\partial \overline{u'^{xy}}}{\partial z} \right]}_{AGSP} \\ & \underbrace{-\overline{u'v'} \frac{\partial \overline{v'_g'^{xy}}}{\partial x}}_{LSP} - \underbrace{\left[\overline{u'u'} \frac{\partial \overline{u'^{xy}}}{\partial x} + \overline{v'v'} \frac{\partial \overline{v'^{xy}}}{\partial y} \right]}_{DSP} + \underbrace{\overline{w'b'^{xy}}}_{BFLUX} \end{aligned} \quad (30)$$

SI grows by extracting the mean kinetic energy from the geostrophic flow at a rate given by the geostrophic shear production, i.e. the term labeled GSP. Ageostrophic shear associated with wind-driven motion energizes the turbulence through ageostrophic shear production (AGSP). Lateral shear instabilities extract kinetic energy from the geostrophic flow at a rate given by lateral shear production (LSP). Kinetic energy can be exchanged between perturbations and the deformation field through the deformation shear production (DSP) term. The vertical buoyancy flux (BFLUX) represents a pathway through which convection and baroclinic instabilities derive kinetic energy from the release of the potential energy of the geostrophic flow.

The time series of spatially averaged EKE sources over the front region are shown in Fig. 11. The geostrophic shear production was large and had a two-layer structure during the restratification stage. The negative values near the surface indicated the dominance of a convection layer in the upper water column, and the positive values indicated that SI was active in the lower water column. The ageostrophic shear production exhibited a reversed two-layer structure compared to the geostrophic shear production. It reduced the growth of SI in the lower water column and eventually dampened SI in the early relaxation of the front. The large values of AGSP near the surface reflected wind-driven Ekman layer turbulence. The lateral and deformation shear productions extracted kinetic energy but had small magnitudes, showing that instabilities caused by lateral and deformation shears were less important. The vertical buoyancy flux was the dominant term in the energy sources and was positive throughout the whole water column. Convection and baroclinic instabilities could have produced the vertical buoyancy flux, but they might not have been the main contributors because SI dominated the restratification stage.

An important fact leading to the large vertical buoyancy flux was that the kinetic and potential energies both increased dramatically during the wind event, which was illustrated with the following volume-integrated energy quantities: mean kinetic energy (MKE), available mean potential energy (AMPE), eddy kinetic energy and available eddy potential energy (AEPE) (Zhang and Gawarkiewicz, 2015):

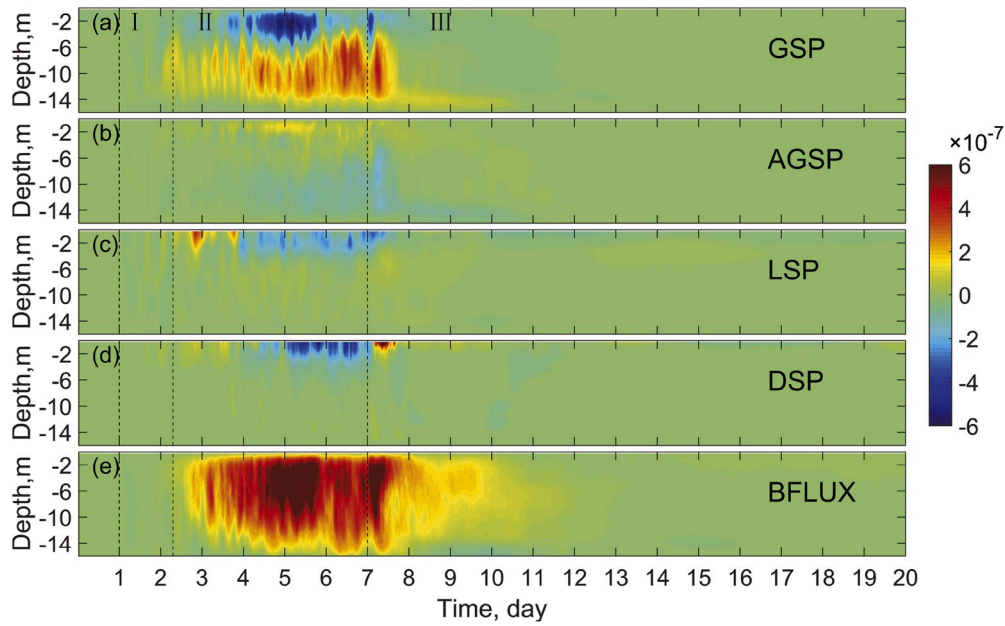


Fig. 11. The time series of eddy kinetic energy sources. (a) geostrophic shear production (GSP), (b) ageostrophic shear production (AGSP), (c) lateral shear production (LSP), (d) deformation shear production (DSP) and (e) vertical buoyancy flux (BFLUX). The parameters were averaged within $0 \text{ km} < x < 17 \text{ km}$ and $20 \text{ km} < y < 200 \text{ km}$. The vertical dashed lines indicate the destratification (I), restratification (II) and relaxation (III) stages.

$$MKE = \frac{\rho_0}{2} \iiint (\bar{u}^{xy^2} + \bar{v}^{xy^2}) dz dy dx \quad (31a)$$

$$AMPE = g \iiint \int_{z-\xi(z)}^z [\bar{\rho}^{xy}(z) - \rho_r(z')] dz' dz dy dx \quad (31b)$$

$$EKE = \frac{\rho_0}{2} \iiint (u^2 + v^2) dz dy dx \quad (31c)$$

$$AEPE = g \iiint \int_{z-\xi(z)}^z [\rho(x, y, z) - \bar{\rho}^{xy}(z')] dz' dz dy dx \quad (31d)$$

where $\xi(z)$ is the vertical displacement of $\bar{\rho}^{xy}$ with respect to the far-field density $\rho_r(z)$ and $\xi'(z)$ is vertical displacement of ρ with respect to $\bar{\rho}^{xy}$. $\xi(z)$ and $\xi'(z)$ are defined to be positive upward. All four of the energy quantities increased during the wind event, and in particular the available mean potential energy and eddy energies evolved with similar trends as the along-shelf freshwater flux during the restratification stage (Fig. 12a). The wind input energy into the river plume and accelerated the coastal current, enhancing the mean kinetic energy. Instabilities developed during the restratification stage and amplified the eddy kinetic energy. The elevated along-shelf freshwater flux not only imposed more buoyancy into the plume, increasing the mean potential energy,

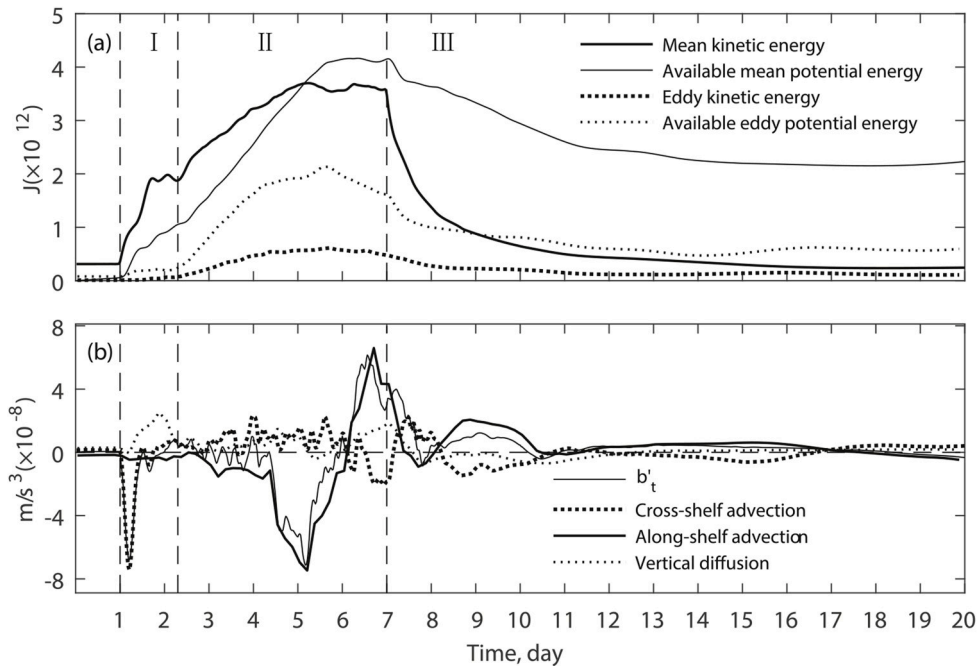


Fig. 12. The time series of (a) volume-integrated energy quantities and (b) diagnostic of buoyancy perturbation conservation equation. The parameters were averaged within $0 \text{ km} < x < 17 \text{ km}$ and $20 \text{ km} < y < 200 \text{ km}$. The dashed vertical lines indicate the destratification (I), restratification (II) and relaxation (III) stages.

but also modified the spatial distribution of the buoyancy in the plume, increasing the eddy potential energy.

The influence of along-shelf freshwater transport on buoyancy perturbations was further examined using the buoyancy perturbation conservation equation:

$$\frac{\partial b'}{\partial t} = - \left[\left(u \frac{\partial b'}{\partial x} - \overline{u^{xy}} \frac{\partial \overline{b^{xy}}}{\partial x} - u' \frac{\partial \overline{b^{xy}}}{\partial x} \right) + \left(w \frac{\partial b'}{\partial z} - \overline{w^{xy}} \frac{\partial \overline{b^{xy}}}{\partial z} - u' \frac{\partial \overline{b^{xy}}}{\partial x} \right) \right] - \left(v \frac{\partial b'}{\partial y} - \overline{v^{xy}} \frac{\partial \overline{b^{xy}}}{\partial y} - v' \frac{\partial \overline{b^{xy}}}{\partial x} \right) + \left[\frac{\partial}{\partial z} \left(K_v \frac{\partial b'}{\partial z} \right) - \frac{\partial}{\partial z} \left(\overline{K_v \frac{\partial \overline{b^{xy}}}{\partial z}} \right) \right] \quad (32)$$

This equation was obtained by subtracting the spatially averaged buoyancy conservation equation from the buoyancy conservation equation. On the right-hand side of the equation, the first term represents cross-shelf advection, the second term represents along-shelf advection and the last term represents vertical diffusion. The time series of the four terms showed that along-shelf advection determined the time change of buoyancy perturbation during the restratification stage, providing further evidence that enhanced along-shelf freshwater flux generates spatial perturbations of buoyancy and hence reinforces the vertical buoyancy flux (Fig. 12b).

4.3. Sensitivity to model configuration

Because idealized numerical models have highly simplified configurations, the findings drawn from those models need to be examined with a wide parameter space of model setup before being generalized and applied to realistic settings. A series of numerical experiments (Table 1) were conducted to confirm the occurrence of symmetric instabilities and restratification during the wind event with different bulge size, grid resolution, bottom disturbances and wind forcing. The relaxation stage favors the development of baroclinic instabilities, but the occurrence of baroclinic instabilities was not further examined here as an in-depth study has been given by Hetland (2017).

Suppressing the bulge of river plumes is critical for increasing along-

shelf freshwater transport. However, the bulge region is rarely distinct in realistic river plumes, although it is widely observed in many idealized numerical simulations (Garvine, 2001). To examine the influence of bulge size on the adjustment of the plume front, the reference case was modified to produce a smaller bulge by enlarging the width of the estuary channel to 80 km. In this small bulge case, the bulge width measured from the coast to the seaward edge was nearly half that in the reference case, and the coastal buoyancy current had a wider width and larger cross-shelf salinity gradient. The front adjustment processes were similar to the reference case as shown by surface salinity, mid-depth vertical velocity and the time series of the PV and Ri_B (Fig. 13a b and Fig. 14a b). It is also noticed that the PV destruction was larger during the wind event in the small bulge case because the bulge was suppressed more significantly and more freshwater was released. An interesting situation following the small bulge is what would happen if the bulge is totally suppressed. The reference case was repeated with a continuous wind forcing that lasted during the entire simulation (i.e. 19 days). Even the bulge was nearly vanished, SI still occurred (Fig. 13c d and Fig. 14a b) because all of the riverine freshwater discharged into coastal currents, providing a persistent buoyancy source.

Small disturbances are typically needed to develop instabilities. The second sensitive experiment was designed by adding noises with a standard deviation equal to 1% of the total depth to the bottom topography to provide some explicit, small, stochastic forcing. However, the bathymetry disturbances did not lead to the early development of instabilities before the abrupt increase in the along-shelf freshwater flux (Fig. 14c d). This further confirmed the role of the along-shelf advection of buoyancy in triggering SI, i.e. reducing the PV and providing disturbances. SI is considered a type of submesoscale instability that is mostly observed in high resolution numerical models. The reference case was repeated with a higher-resolution model grid that has a horizontal grid size of 500 m. The results showed few differences in the front adjustment processes (Fig. 14c d), although more intense filaments appeared in the restratification stage. Despite the relatively large grid size (e.g. 1 km) in the reference case, the Ro in deed approached 1.0, showing that the 1.0

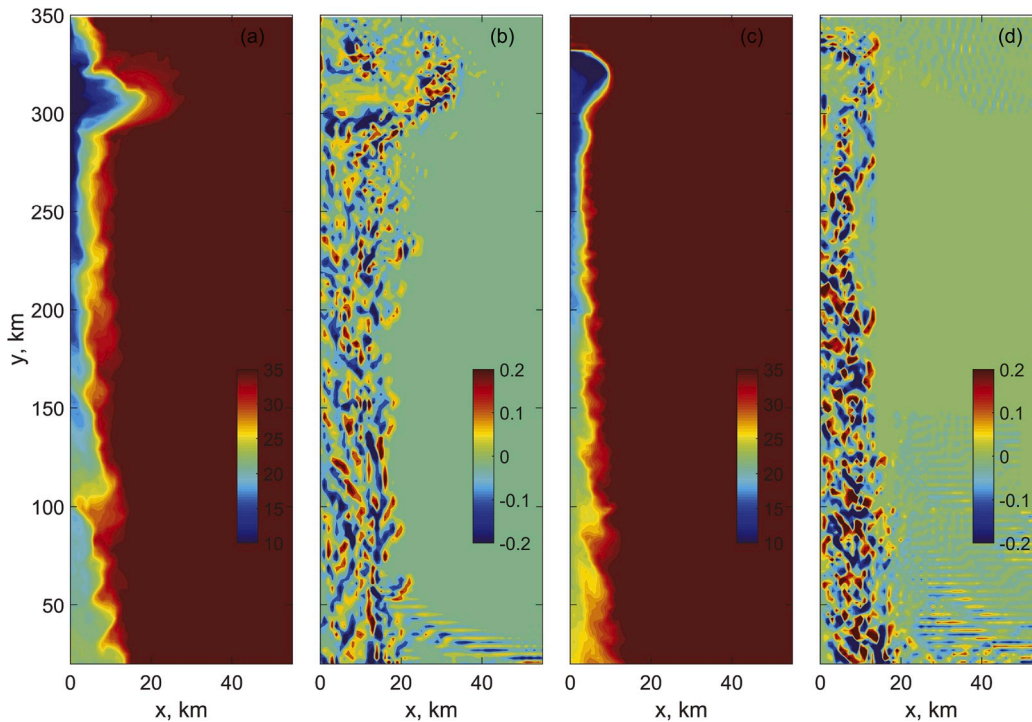


Fig. 13. Surface salinity and mid-depth vertical velocity to represent the restratification stages for the experiments with small bulge (a, b) and with continuous wind forcing (c, d). The results were taken at time $t = 5$ days for the small bulge case, and time $t = 19$ days for the continuous wind forcing case. Salinity is measured in psu and velocity in mm/s.

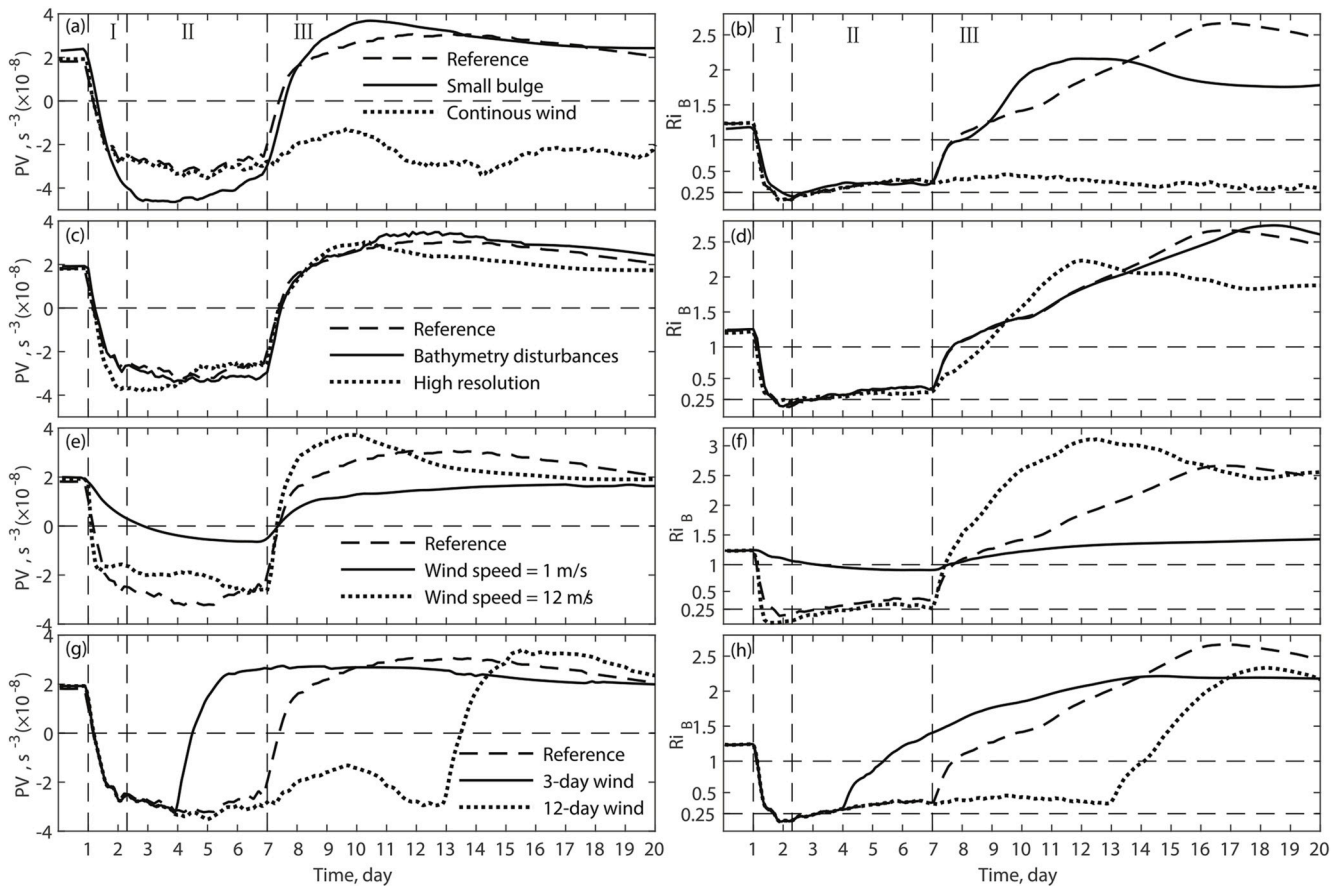


Fig. 14. The time series of the (a) potential vorticity (PV) and (b) bulk Richardson number (Ri_B) for the reference and sensitivity experiments of wind speed. The parameters were averaged within $0 \text{ km} < x < 17 \text{ km}$ and $20 \text{ km} < y < 200 \text{ km}$. The dashed vertical lines indicate the destratification (I), restratification (II) and relaxation (III) stages in the reference case.

km grid size could allow SI to develop.

Wind strength affects the adjustment of river plume fronts. The reference case was compared with two other cases, one having a weak wind with a speed of 1 m/s and the other having a strong wind with a speed of 12 m/s. The strong wind led to early restratification, while the weak wind delayed the occurrence of instabilities (Fig. 14e f). The weak wind could not produce a well-mixed front and push the convective layer on the seaward side of the front, but it still led to SI as long as the enhanced along-shelf buoyancy flux further reduced the PV and Ri_B to certain levels. Whether the wind is strong or weak, the plume front always goes through the three adjustment stages. The wind duration mainly modified the length of restratification, as shown from the comparison of sensitivity experiments that have the same wind speed but different wind durations (Fig. 14g h). The results showed that longer wind duration leads to longer restratification.

5. Conclusions

In response to a downwelling-favorable event, the adjustment of river plume fronts went through three stages: destratification and restratification during the wind event and relaxation after the wind event. The wind-driven Ekman transport suppressed the front width and drove a downwelling cross-shelf circulation that steepened the isohalines and tended to generate a well-mixed front if the wind was strong. Based on the potential energy anomaly conservation, a time scale of destratification was developed. It is the time that the Ekman transport takes to suppress the front by the distance from the foot to the offshore edge of the front. When the destratification time is shorter than the wind duration, the wind is able to complete the destratification process and is

considered a strong wind. The front adjustment continued and instabilities occurred after the destratification. SI dominated the rest of the wind event and restratified the front through the eddy advection. After the wind decayed, the SI gradually ceased, but the front was still unstable due to the subsequent baroclinic instabilities that further stratified the front during the relaxation stage.

Down-front winds have been recognized as a driver of SI through the Ekman transport-induced cross-front circulation that pushes the PV in the front toward the opposite of the Coriolis parameter. Because of the constraint of sloping bottom, the cross-front circulation tends to be restricted on the seaward side of the plume front, and, therefore, cannot further reduce PV. However, the existence of riverine buoyancy sources in river plumes allows the down-front winds to enhance the along-shelf buoyancy flux that on one hand increases the cross-shelf buoyancy gradient, reducing the PV, and on the other hand generates buoyancy disturbances, increasing the vertical buoyancy flux. The combined effect is to provide a negative along-shelf PV flux. Both Ekman buoyancy flux and the negative along-shelf PV flux triggered and sustained SI during the restratification stage and the latter is the main driver, confirming the importance of along-shelf processes in the plume front adjustment.

A series of sensitivity experiments were carried out and confirmed SI can occur during the wind event in a wide range of model parameter space. The development of baroclinic instability during the relaxation, however, is restricted by the constraint that eddies must fit within the plume front, such that it might be not always occurred. Because of the highly simplified model configurations applied in this generic study, the conclusions drawn from this study still need further examination, particularly through realistic numerical simulations and field observations.

Declaration of competing interest

All authors declare that we have no financial and personal relationships with other people or organizations that can inappropriately influence our work, there is no professional or other personal interest of any nature or kind in any product, service and/or company that could be construed as influencing the position presented in, or the review of, the manuscript entitled.

Acknowledgments

This work is supported by the National Basic Research Program of China (grant No. 2015CB954000) and the National Natural Science Foundation of China (grant No. 41476004). We thank the anonymous reviewers for the insightful comments that helped improve this work.

References

- Allen, J.S., Newberger, P.A., 1996. Downwelling circulation on the Oregon continental shelf. Part I: response to idealized forcing. *J. Phys. Oceanogr.* 26, 2011–2035. [https://doi.org/10.1175/1520-0485\(1996\)026<2011:DCOTOC>2.0.CO;2](https://doi.org/10.1175/1520-0485(1996)026<2011:DCOTOC>2.0.CO;2).
- Barth, J.A., 1994. Short-wave length instabilities on coastal jets and fronts. *J. Geophys. Res.* 99, 16095. <https://doi.org/10.1029/94jc01270>. <https://search.crossref.org/?q=Barth+JA+%281994%29+Short-wave+length+instabilities+on+coastal+jets+and+fronts.+J.+Geophys.+Res.+99%3A+16095>.
- Blumsack, S.L., Gierasch, P.J., 1972. Mars: the effects of topography on baroclinic instability. *J. Atmos. Sci.* 29, 1081–1089. [https://doi.org/10.1175/1520-0469\(1972\)029<1081:MTEOTO>2.0.CO;2](https://doi.org/10.1175/1520-0469(1972)029<1081:MTEOTO>2.0.CO;2).
- Boccaletti, G., Ferrari, R., Fox-Kemper, B., 2007. Mixed layer instabilities and restratification. *J. Phys. Oceanogr.* 37, 2228–2250. <https://doi.org/10.1175/JPO3101.1>. <http://journals.ametsoc.org/doi/abs/10.1175/JPO3101.1>.
- Burchard, H., Hofmeister, R., 2008. A dynamic equation for the potential energy anomaly for analysing mixing and stratification in estuaries and coastal seas. *Estuar. Coast Shelf Sci.* 77, 679–687. <https://doi.org/10.1016/j.ecss.2007.10.025>.
- Capet, X., McWilliams, J.C., Molemaker, M.J., Shchepetkin, A.F., 2008. Mesoscale to submesoscale transition in the California current system. Part III: energy balance and flux. *J. Phys. Oceanogr.* 38, 2256–2269. <https://doi.org/10.1175/2008JPO3810.1>.
- Chao, S.-Y., 1988. Wind-driven motion of estuarine plumes. *J. Phys. Oceanogr.* 18, 1144–1166. [https://doi.org/10.1175/1520-0485\(1988\)018<1144:WDMOEP>2.0.CO;2](https://doi.org/10.1175/1520-0485(1988)018<1144:WDMOEP>2.0.CO;2).
- Chapman, D.C., Lentz, S.J., 1994. Trapping of a coastal density front by the bottom boundary layer. *J. Phys. Oceanogr.* 24, 1464–1479. [https://doi.org/10.1175/1520-0485\(1994\)024<1464:TOACDF%3E2.0.CO](https://doi.org/10.1175/1520-0485(1994)024<1464:TOACDF%3E2.0.CO).
- Chen, S.-Y., Chen, S.-N., 2017. Generation of upwelling circulation under downwelling-favorable wind within bottom-attached, buoyant coastal currents. *J. Phys. Oceanogr.* 47, 2499–2519. <https://doi.org/10.1175/JPO-D-16-0271.1>.
- Choi, B.-J., Wilkin, J.L., 2007. The effect of wind on the dispersal of the Hudson River Plume. *J. Phys. Oceanogr.* 37, 1878–1897. <https://doi.org/10.1175/JPO3081.1>.
- de Boer, G.J., Pietrzak, J.D., Winterwerp, J.C., 2008. Using the potential energy anomaly equation to investigate tidal straining and advection of stratification in a region of freshwater influence. *Ocean Model.* 22, 1–11. <https://doi.org/10.1016/j.ocemod.2007.12.003>.
- D'Asaro, E., Lee, C., Rainville, L., Harcourt, R., Thomas, L., 2011. Enhanced turbulence and energy dissipation at ocean fronts. *Science* 332, 318–322. <https://doi.org/10.1126/science.1201515>.
- Hickey, B.M., et al., 2010. River influences on shelf ecosystems: introduction and synthesis. *J. Geophys. Res. Ocean* 115, 1–26. <https://doi.org/10.1029/2009JC005452>.
- Fewings, M., Lentz, S.J., Fredericks, J., 2008. Observations of cross-shelf flow driven by cross-shelf winds on the inner continental shelf. *J. Phys. Oceanogr.* 38, 2358–2378. <https://doi.org/10.1175/2008JPO3990.1>.
- Fong, D.A., Geyer, W.R., 2001. Response of a river plume during an upwelling favorable wind event. *J. Geophys. Res.* 106, 1067–1084. <https://doi.org/10.1029/2000JC900134>.
- Fong, D.A., Geyer, W.R., 2002. The alongshore transport of freshwater in a surface-trapped river plume. *J. Phys. Oceanogr.* 32, 957–972. [https://doi.org/10.1175/1520-0485\(2002\)032<0957:TATOFI>2.0.CO;2](https://doi.org/10.1175/1520-0485(2002)032<0957:TATOFI>2.0.CO;2).
- Fong, D.A., Geyer, W.R., Signell, R.P., 1997. The wind-forced response on a buoyant coastal current: observations of the western Gulf of Maine plume. *J. Mar. Syst.* 12, 69–81. [https://doi.org/10.1016/S0924-7963\(96\)00089-9](https://doi.org/10.1016/S0924-7963(96)00089-9).
- Gan, J., Li, L., Wang, D., Guo, X., 2009. Interaction of a river plume with coastal upwelling in the northeastern South China Sea. *Continental Shelf Res.* 29, 728–740. <https://doi.org/10.1016/j.csr.2008.12.002>.
- Garvine, R.W., 2001. The impact of model configuration in studies of buoyant coastal discharge. *J. Mar. Res.* 59, 193–225. <https://doi.org/10.1357/002224001762882637>.
- Haine, T.W.N., Marshall, J., 1998. Gravitational, symmetric, and baroclinic instability of the ocean mixed layer. *J. Phys. Oceanogr.* 28, 634–658. [https://doi.org/10.1175/1520-0485\(1998\)028<0634:GSABIO>2.0.CO;2](https://doi.org/10.1175/1520-0485(1998)028<0634:GSABIO>2.0.CO;2).
- Haynes, P.H., McIntyre, M.E., 1987. On the evolution of vorticity and potential vorticity in the presence of diabatic heating and frictional or other forces. *J. Atmos. Sci.* 44, 828–841. [https://doi.org/10.1175/1520-0469\(1987\)044<0828:OTEOVA>2.0.CO;2](https://doi.org/10.1175/1520-0469(1987)044<0828:OTEOVA>2.0.CO;2).
- Hetland, R.D., 2017. Suppression of baroclinic instabilities in buoyancy-driven flow over sloping bathymetry. *J. Phys. Oceanogr.* 47, 49–68. <https://doi.org/10.1175/JPO-D-15-0240.1>.
- Horner-Devine, A.R., Hetland, R.D., MacDonald, D.G., 2015. Mixing and transport in coastal River Plumes. *Annu. Rev. Fluid Mech.* 47, 569–594. <https://doi.org/10.1146/annurev-fluid-010313-141408>.
- Hoskins, B.J., 1974. The role of potential vorticity in symmetric stability and instability. *Q. J. R. Meteorol. Soc.* 100, 480–482. <https://doi.org/10.1002/qj.49710042520>.
- Jickells, T.D., 1998. Nutrient biogeochemistry of the coastal zone. *Science* 281, 217–222. <https://doi.org/10.1126/science.281.5374.217>.
- Johnson, D.R., Weidemann, A., Arnone, R., Davis, C.O., 2001. Chesapeake Bay outflow plume and coastal upwelling events: physical and optical properties. *J. Geophys. Res.* 106, 11613. <https://doi.org/10.1029/1999JC000185>.
- Jurisa, J.T., Chant, R.J., 2013. Impact of offshore winds on a buoyant River Plume system. *J. Phys. Oceanogr.* 43, 2571–2587. <https://doi.org/10.1175/JPO-D-12-0118.1>.
- Large, W.G., Pond, S., 1981. open ocean momentum flux measurements in moderate to strong winds. *J. Phys. Oceanogr.* 11, 324–336. [https://doi.org/10.1175/1520-0485\(1981\)011<0324:OOMFMI>2.0.CO;2](https://doi.org/10.1175/1520-0485(1981)011<0324:OOMFMI>2.0.CO;2).
- Lentz, S., 2004. The response of buoyant coastal plumes to upwelling-favorable winds. *J. Phys. Oceanogr.* 34, 2458–2469. <https://doi.org/10.1175/JPO2647.1>. <http://journals.ametsoc.org/doi/abs/10.1175/JPO2647.1>.
- Lentz, S., Largier, J.L., 2006. The influence of wind forcing on the Chesapeake Bay buoyant coastal current. *J. Phys. Oceanogr.* 36, 1305–1316. <http://journals.ametsoc.org/doi/pdf/10.1175/JPO2909.1>.
- Marshall, J.C., Nurser, A.J.G., 1992. Fluid dynamics of oceanic thermocline ventilation. *J. Phys. Oceanogr.* 22, 583–595. [https://doi.org/10.1175/1520-0485\(1992\)022<0583:FDOOTV>2.0.CO;2](https://doi.org/10.1175/1520-0485(1992)022<0583:FDOOTV>2.0.CO;2).
- Matano, R.P., Palma, E.D., 2013. The impact of boundary conditions on the upstream spreading of bottom-trapped plumes. *J. Phys. Oceanogr.* 43, 1060–1069. <https://doi.org/10.1175/JPO-D-12-0116.1>.
- McWilliams, J.C., 2016. Submesoscale currents in the ocean. *Proc. R. Soc. A Math. Phys. Eng. Sci.* 472, 20160117. <https://doi.org/10.1098/rspa.2016.0117>.
- McWilliams, J.C., 2019. A survey of submesoscale currents. *Geosci. Lett.* 6, 3. <https://doi.org/10.1186/s40562-019-0133-3>.
- Moffat, C., Lentz, S., 2012. On the response of a buoyant plume to downwelling-favorable wind stress. *J. Phys. Oceanogr.* 42, 1083–1098. <https://doi.org/10.1175/JPO-D-11-015.1>.
- Münchow, A., Garvine, R.W., 1993. Dynamical properties of a buoyancy-driven coastal current. *J. Geophys. Res.* 98, 20063. <https://doi.org/10.1029/93JC02112>.
- Rogers-Cotrone, J., Yankovsky, A.E., Weingartner, T.J., 2008. The impact of spatial wind variations on freshwater transport by the Alaska Coastal Current. *J. Mar. Res.* 66, 899–925.
- Shchepetkin, A., McWilliams, J.C., 2003. The Regional Ocean Modeling System: a split-explicit, free-surface, topography-following coordinates ocean model. *Ocean Model.* 9, 347–404.
- Simpson, J.H., Brown, J., Matthews, J., Allen, G., 1990. Tidal straining, density currents, and stirring in the control of estuarine stratification. *Estuaries* 13, 125–132. <https://doi.org/10.2307/1351581>.
- Spall, M.A., Thomas, L.N., 2016. Downfront winds over buoyant coastal plumes. *J. Phys. Oceanogr.* 46, 3139–3154. <https://doi.org/10.1175/JPO-D-16-0042.1>.
- Stone, P.H., 1966. On non-geostrophic baroclinic stability. *J. Atmos. Sci.* 23, 390–400. [https://doi.org/10.1175/1520-0469\(1966\)023<0390:ONGBS>2.0.CO;2](https://doi.org/10.1175/1520-0469(1966)023<0390:ONGBS>2.0.CO;2).
- Taylor, J.R., Ferrari, R., 2010. Buoyancy and wind-driven convection at mixed layer density fronts. *J. Phys. Oceanogr.* 40, 1222–1242. <https://doi.org/10.1175/2010JPO4365.1>.
- Thomas, L.N., 2005. Destruction of potential vorticity by winds. *J. Phys. Oceanogr.* 35, 2457–2466. <https://doi.org/10.1175/JPO2830.1>.
- Thomas, L.N., Lee, C.M., 2005. Intensification of ocean fronts by down-front winds. *J. Phys. Oceanogr.* 35, 1086–1102. <https://doi.org/10.1175/JPO2737.1>.
- Thomas, L.N., Taylor, J.R., 2010. Reduction of the useable wind-work on the general circulation by forced symmetric instability. *Geophys. Res. Lett.* 37, 1–5. <https://doi.org/10.1029/2010GL044680>.
- Thomas, L.N., Tandon, A., Mahadevan, A., 2008. Submesoscale processes and dynamics. In: *Geophysical Monograph Series*, vol. 177. American Geophysical Union, pp. 17–38. <https://doi.org/10.1029/177gm04>. In: <https://search.crossref.org/?q=Thomas+LN%2C+Tandon+A%2C+Mahadevan+A+%282008%29+Submesoscale+processes+and+dynamics.+Geophysical+Monograph+Series%2C+American+Geophysical+Union%2C+Vol.+vol.+177%3A+17%2E2%80%9338>.
- Thomas, L.N., Taylor, J.R., Ferrari, R., Joyce, T.M., 2013. Symmetric instability in the gulf stream. *Deep Res. Part II Top Stud. Oceanogr.* 91, 96–110. <https://doi.org/10.1016/j.dsr2.2013.02.025>.
- Whitney, M.M., Garvine, R.W., 2005. Wind influence on a coastal buoyant outflow. *J. Geophys. Res. Ocean* 110, 1–15. <https://doi.org/10.1029/2003JC002261>.
- Williams, W.J., Weingartner, T.J., Hermann, A.J., 2010. Idealized two-dimensional modeling of a coastal buoyancy front, or River Plume, under downwelling-favorable wind forcing with application to the Alaska coastal current. *J. Phys. Oceanogr.* 40, 279–294. <https://doi.org/10.1175/2009JPO4206.1>.
- Zhang, W.G., Gawarkiewicz, G.G., 2015. Length scale of the finite-amplitude meanders of shelfbreak fronts. *J. Phys. Oceanogr.* 45, 2598–2620. <https://doi.org/10.1175/JPO-D-14-0249.1>.